Numerical simulation of the impact of a gas jet on a free water surface

Ward Haegeman, Clément Le Touze, Joël Dupays, Marc Massot

Numerical simulation of the impact of a gas jet on a free water surface

Ward Haegeman[1,2], Clément Le Touze[2], Joël Dupays[2] and Marc Massot[1]

[1] CMAP, CNRS, École polytechnique, Institut Polytechnique de Paris, Palaiseau, 91120, France

[2] DMPE, ONERA, Université Paris Saclay, F-91123 Palaiseau - France

ward.haegeman@onera.fr

Keywords: Impinging jets, Diffuse interface models, Low-Mach schemes, Relaxation schemes.

Abstract

In this work, we are interested in the numerical simulation of a high-speed hot jet impinging on a free liquid surface at rest by means of diffuse interface models. We first consider the case of a low-temperature subsonic jet; a 4-equation model is used on a 2D axi-symmetric set-up. Turbulence is accounted for by solving the Reynolds averaged equations and using a $k-\omega$ turbulence model. Numerical results are evaluated by comparing the depth of the cavity formed in the liquid surface to the predicted values using theoretical models from the literature. We then consider the case of a high-temperature jet. We start by showing the limits of the previous model as it relies on a thermal equilibrium assumption between the liquid and gas phases which is no longer valid. A 5-equation model that does not rely on this assumption is presented. Both models are compared numerically on a simplified set-up.

Introduction

The objective of the present study is to investigate the numerical simulation of a supersonic hot jet impinging on a free liquid surface initially at rest. This type of two-phase flow is of particular interest in defence applications but also to several industries such as the steel industry where supersonic jets are used in the oxidation process.

Several methods allow the numerical simulation of two-phase flows, such as the Volume of Fluid or the Level-Set method which allow for accurate capturing of the interface motion (Mirjalili et al. 2017). The flows we are interested in are quite challenging as they contain a wide range of scales (both in time and space) and complex physics (wide range of Mach numbers, strong temperature gradients, evaporation, water splashing, ...). Since a Direct Numerical Simulation at industrial scale is out of reach, predictive reduced-order models are required. We focus on diffuse interface models which have been chosen for their robustness and flexibility with respect to the flow topology. Several diffuse interface models exist in the literature, one of the most complete ones is a 7-equation model* (Baer and Nunziato 1986) which allows the two phases to be locally out of mechanical and thermal equilibrium. It is often practical to assume that some quantities will remain at equilibrium during the flow, thus reducing the number of variables and leading to a hierarchy of models. Within the development of the CEDRE code at ONERA, the most advanced model in terms of development is a 4-equation model† (Le Touze 2015) which assumes local equilibrium between the pressures, velocities and temperatures. A 5-equation model (Cordesse 2020) which does not assume local thermal equilibrium between phases is also under development. Since these models do not allow to compute the finest flow features, they can be enriched through the modelling of sub-scale quantities, see for instance Cordesse (2020); Di Battista (2021) but also the current works of A. Loison at CMAP (Loison et al. 2023a,b).

Working towards our goal which is the numerical simulation of a high-temperature, supersonic gas jet impinging on a resting free water surface, in this paper we first consider the case of a subsonic jet. We start by studying the low-temperature‡ case which has been the subject of a great many studies over the years. Assuming a stationary cavity and neglecting viscosity as well as surface tension, Banks and Chandrasekhara (1963) obtained a relationship between cavity depth and jet momentum. This analytical model was compared to experimental measurements of cavity depths by means of photographs, it was shown that the data is in good agreement with the theoretical predictions. Similar experiments were carried out by Cheslak et al. (1969) using fast-setting cement in order to get more accurate measurements which also validated theoretical predictions. Rosler and Stewart (1968) showed that low-velocity jets lead to stationary and axisymmetric cavities. As the jet velocity increases, the cavity reaches a length to width ratio for which it becomes unstable and starts to oscillate. When the jet velocity is even further

*2 mass, 2 momentum, 2 energy conservation equation and 1 equation on the volume fraction.

†2 mass conservation equations, 1 momentum and 1 energy conservation equations.

‡by low-temperature we mean that the jet's temperature is the same as the liquid's and such that no phase change occurs.

increased, air bubbles penetrate the liquid and splashing water droplets appear. A linear relation between surface tension and the squares of the critical jet velocities governs the transition between these different dynamics. Molloy (1970) identified three cavity regimes: dimpling, splashing and penetrating. The case we are ultimately interested in corresponds to the penetrating regime, the results presented in this paper however correspond to the dimpling regime.

In order to obtain predictive numerical simulations, the jet's velocity profile must be computed accurately. As ultimately, we aim at considering high jet Mach numbers M_{jet}, compressibility effects must be taken into account into our model. This is not the case when considering small jet Mach numbers for which incompressible models can be used and have shown good results (Nguyen and Evans 2006; Adib et al. 2018). However, as the liquid has an extremely low compressibility and is initially at rest, we are subject to the well-known issue of compressible solvers failing in the low-Mach regime. Using a low-Mach correction, we numerically show the 4-equation model's capability to retrieve the correct dynamics of the cavity in the low-velocity and low-temperature jet regime as the results are compared to theoretical predictions. Next we show that the local thermal equilibrium imposed by this 4-equation model limits its capabilities to treat the case of a high-temperature jet, thus justifying the development of a 5-equation model which does not rely on such an assumption. We assess the capabilities of the new model on a simplified set-up.

The outline of this paper is the following. Section 1 is devoted to the results obtained for the simplified case of a cold subsonic jet using a 4-equation model. First, the model and the numerical methods used are presented, the low-Mach correction used is described and its effects on the numerical stability of the computations are shown. Next the numerical set-up and the obtained results are presented and compared to theoretical predictions. Section 2 concerns the case of a hot jet, we start by showing that the thermal equilibrium assumption on which the 4-equation model relies is no longer viable, and then consider a 5-equation model for which the two phases are allowed to be locally out of thermal equilibrium. The model and its numerical methods are presented and we propose a comparison to the previous model on a simplified set-up.

1 Simulation of a low-temperature impinging jet

1.1 Presentation of a 4-equation model

The 4-equation model (Le Touze 2015) assumes that locally both phases share the same temperature, velocity and pressure. Its vector of conservative variables writes $\boldsymbol{Q} = (\rho Y_{j,k},\ \rho \boldsymbol{u},\ \rho E)^{\intercal}$ with ρ, $\boldsymbol{u}$ and E representing the mixture's density, velocity and specific total energy respectively. The specific internal energy is denoted $e := E - \frac{1}{2}u^2$. Variables $Y_{j,k}$ correspond to the mass fractions of the different species with respect to the mixture, here $k \in \{\text{g},\ \ell\}$ refers to either the gaseous or liquid phase while $j \in [\![1,\ n_k]\!]$ is used for indexing the species within phase k. The total mass fractions of each phase are given by $Y_k = \sum_j Y_{j,k}$ and sum up to one. In conservative form, the system writes

$$\partial_t \boldsymbol{Q} + \nabla \cdot (\boldsymbol{f_c} + \boldsymbol{f_d} + \mathbf{f}_{\boldsymbol{\sigma}}) = \boldsymbol{S}, \tag{1}$$

with $\boldsymbol{f_c}$ the convective flux tensor which corresponds to the standard compressible multi-species Euler fluxes. Tensors $\boldsymbol{f_d}$ and $\boldsymbol{f_\sigma}$ respectively represent diffusive fluxes (possibly including RANS or LES turbulent diffusion) and surface tension fluxes using the Continuum Surface Stress flux expression, while $\boldsymbol{S}$ represents source terms here only gravity.

Thermodynamic closure is obtained by computing the mixture pressure and temperature. Provided that the equations of state $e_k^{\text{EOS}}(p,T)$ and $v_k^{\text{EOS}}(p,T)$, expressing the internal energy and specific volume of each pure phase are given, the mixture pressure and temperature are p, T such that

$$\begin{cases} \rho Y_{\text{g}} e_{\text{g}}^{\text{EOS}}(p,T) + \rho Y_\ell e_\ell^{\text{EOS}}(p,T) = \rho e, \\ \underbrace{\rho Y_{\text{g}} v_{\text{g}}^{\text{EOS}}(p,T)}_{=\alpha_{\text{g}}} + \underbrace{\rho Y_\ell v_\ell^{\text{EOS}}(p,T)}_{=\alpha_\ell} = 1. \end{cases} \tag{2}$$

As indicated by the under-brackets, this also allows to compute the volume fraction $\alpha_k := Y_k \frac{\rho}{\rho_k}$ of each phase. In our case, we consider a mixture of perfect gases (air and nitrogen), denoting $y_{j,k}$ the mass fraction of the j^{th} species with respect to its phase, we have

$$v_{\text{g}}^{\text{EOS}} = \frac{RT}{p} \sum_{j=1}^{n_{\text{g}}} \frac{y_{j,\text{g}}}{W_j}, \qquad e_{\text{g}}^{\text{EOS}} = \sum_{j=1}^{n_{\text{g}}} c_{v,j,\text{g}} y_{j,\text{g}} T, \tag{3}$$

with W_j and $c_{v,j,\text{g}}$ the molar mass and specific heat capacity at constant volume of the j^{th} species respectively and R the universal gas constant.

The liquid phase is considered pure *ie* composed by only water. Described by a compressible liquid law obtained through the linearisation of the specific volume near a pressure-temperature reference point $(p_0,\ T_0)$, its equation of state writes

$$v_\ell^{\text{EOS}} = v_{0,\ell} \frac{1 + \alpha_{0,\ell}(T - T_0)}{1 + \beta_{0,\ell}(p - p_0)}. \tag{4}$$

Here $v_{0,\ell}$ is the liquid's specific volume while $\alpha_{0,\ell}$ and $\beta_{0,\ell}$ are its thermal expansion and isothermal compressibility coefficients all taken at the reference point. Knowing the expression of the specific heat $T \mapsto c_{v,\ell}(T)$ for the liquid as well as the specific

internal energy $e_{0,\ell}$ of the reference state, the expression of $e_\ell^{\mathrm{EOS}}(p,T)$ can be derived from (4) using classical thermodynamic relations. For our application, we have chosen $p_0 = 101325$ Pa, $T_0 = 298.15$ K and $v_{0,\ell} = 10^{-3}$ m^3/kg. Using $\alpha_{0,\ell} = 2.5\cdot10^{-4}$ 1/K and $\beta_{0,\ell} = 5.0\cdot10^{-10}$ 1/Pa, as well as $c_p^{\mathrm{mol}} = 75.3$ J/(K mol) and $W_{0,\ell} = 1.8\cdot10^{-2}$ kg/mol, yields the sound velocity $c_{\mathrm{water}} = 1420$ m/s at reference conditions. Since the liquid's equation of state is obtained through a linearisation at a reference point, its physical validity is restricted and not suited for strong temperature gradients. The development of a robust equation of state valid over a wider range of temperatures will be included in future works.

1.2 Numerical discretization of the governing equations

As our end-goal is to simulate a system with complex physics containing stiff source terms modelling exchanges between phases and relaxation terms with small parameters, we aim for a robust method compatible with general meshes. This is why we have opted for the method of lines, which allows the use of different time integrators, each adapted to specific parts of the system through the use of operator splitting techniques. This will be useful once stiff source terms are included. Space discretization is achieved through a finite-volume method with a multislope MUSCL reconstruction (Le Touze 2015) using the Van Leer limiter. Interface fluxes are computed with a HLLC-type Riemann solver (Toro et al. 1994). The resulting ODE, which we write

$$\frac{\mathrm{d}}{\mathrm{d}t}\mathcal{Q} = \mathbb{F}(\mathcal{Q}), \tag{5}$$

is then solved numerically using a linearly implicit Euler method such that

$$\mathcal{Q}^{n+1} = \mathcal{Q}^n + \Delta t\left[\mathrm{Id} - \Delta t \mathrm{D}\mathbb{F}\left(\mathcal{Q}^n\right)\right]^{-1}\mathbb{F}\left(\mathcal{Q}^n\right). \tag{6}$$

This method is obtained by linearising the nonlinear system given by the implicit Euler method. This strategy can be applied to any diagonally implicit Runge-Kutta method and the resulting methods are referred to as Rosenbrock methods (Hairer and Wanner 1996). The resulting linear system is solved using the GMRES method.

Other time integrators have also been tested such as a 2nd-order linearly-implicit Runge-Kutta method or explicit methods such as the Strong Stability Preserving (SSP) Runge-Kutta methods. For an extensive review of the SSP methods, we refer to the book of Gottlieb et al. (2011). We simply recall that these methods are obtained by a series of convex combinations of explicit Euler steps such that if under a suitable time-step restriction, the explicit Euler step satisfies a stability condition for a given norm (semi-norm or scalar convex function such as total variation), then the explicit SSP scheme will also satisfy a stability property under a similar time-step restriction, as will all intermediate stages. For some Runge-Kutta schemes (in particular those with negative coefficients), spurious oscillations in the intermediate stages can cause great difficulties, for instance when negative densities appear, this is thus avoided by SSP schemes. An interesting strategy is the use of an increased number of stages in order to allow for higher time-steps (Ruuth et al. 2002). For instance the explicit 2nd-order SSP Runge-Kutta scheme with m stages has the following Butcher table

$$\begin{array}{c|cccccc}
0 & 0 & \dots & \dots & \dots & 0 \\
\frac{1}{m-1} & \frac{1}{m-1} & 0 & \dots & \dots & 0 \\
\frac{2}{m-1} & \frac{1}{m-1} & \frac{1}{m-1} & 0 & \dots & 0 \\
\vdots & \vdots & \vdots & \ddots & \ddots & \vdots \\
1 & \frac{1}{m-1} & \frac{1}{m-1} & \dots & \frac{1}{m-1} & 0 \\
\hline
 & \frac{1}{m} & \frac{1}{m} & \dots & \dots & \frac{1}{m}
\end{array} \qquad m \geq 2, \tag{7}$$

which in the case $m = 2$ reduces to the classical Heun method while allowing the use of time steps corresponding to larger CFL numbers when $m > 2$. A low storage algorithm for the implementation of these methods is given in Ketcheson (2008).

Since we want to reach a steady state solution, implicit methods allowing for higher CFL numbers have been favoured. For the cases presented in this paper, the use of a 1st-order time integrator has proved sufficient as the numerical errors are dominated by those of the space discretization. This is because in the cold subsonic jet case, the interface dynamics are relatively slow while the stability constraints lead to very small time-steps even when using an implicit method (recall that no preconditioning techniques to artificially reduce the water sound velocity have been used). However 2nd-order space accuracy did prove necessary to reduce the non-physical spreading of the interface which was caused by excessive numerical dissipation and which dampens the dynamics.

1.3 Behaviour of compressible models in the low-Mach limit

The Mach number $M := \frac{u}{c}$, ratio between the velocity u and sound speed c determines the importance of compressibility effects. As the Mach number tends to zero, the compressible equations tend to the incompressible ones. However, at the discrete

level it is well-known that the classical finite volume schemes for the compressible equations become very stiff at low-Mach numbers and thus these schemes suffer from a loss of accuracy and fail to capture the incompressible regime unless an extremely refined discretization is used. Before presenting the low-Mach correction we applied to the aforementioned scheme and showing its effects on the computation, we briefly recall why the classical finite volume schemes for the compressible Euler equations break down in the low-Mach regime.

When the compressible Euler equations are written in non-dimensional form using a convective time-scaling — that is to say that $\hat{t} = \hat{x}/\hat{u}$ rather than $\hat{t} = \hat{x}/\hat{c}$ which would represent an acoustic time scaling (with $\hat{\bullet}$ denoting reference quantities) — the momentum equation becomes

$$\frac{\partial \rho \boldsymbol{u}}{\partial t} + \boldsymbol{\nabla} \cdot (\rho \boldsymbol{u} \otimes \boldsymbol{u}) + \frac{1}{M^2} \boldsymbol{\nabla} p = \boldsymbol{0}, \tag{8}$$

with ρ, $\boldsymbol{u}$, p the non-dimensional density, velocity and pressure fields and M the reference Mach number. In the low-Mach regime *ie* $M \ll 1$, looking for the solution as a formal power series of the Mach number *ie* $\mathcal{X} = \sum_{n \geq 0} \mathcal{X}_n M^n$ for $\mathcal{X} \in \{\rho, \boldsymbol{u}, p\}$ yields that the zero-th order terms solve the incompressible Euler equations and that pressure fluctuations are of 2^{nd} order ($\sim M^2$). However, as shown by Guillard and Viozat (1999), using a Roe scheme on a 2D cartesian grid, the numerical solution exhibits pressure fluctuations of order 1 ($\sim M$) which pollute the numerical solution. Through a Hodge-Helmholtz decomposition (*ie* writing the velocity field as the sum of an incompressible flow and a potential flow), Dellacherie (2010) linked the low-Mach inaccuracies to the behaviour of the scheme for the linear wave equation, and in particular to the numerical diffusion of the scheme using a first-order modified equation analysis. The analysis shows that accuracy at low-Mach numbers can be retrieved by a modification of the numerical viscosity in the momentum equation and several such fixes exist in the literature (Rieper 2011; Dellacherie 2010). Although, these results are mainly derived for the two-dimensional Euler equations without body forces, numerical tests show that they still shed some light on the more general case that we consider, that of an axi-symmetric turbulent multiphase system (similar to the multi-species Navier-Stokes equations) on unstructured meshes.

In order to describe our low-Mach correction, we recall that the HLLC-type Riemann solver provides approximate solutions to the Riemann problem between states $\boldsymbol{Q}_L$ and $\boldsymbol{Q}_R$ through a succession of four constant states $\boldsymbol{Q}_L$, $\boldsymbol{Q}_L^\star$, $\boldsymbol{Q}_R^\star$, $\boldsymbol{Q}_R$ separated by three waves with speeds $S_L \leq S_M \leq S_R$. Intermediate states are computed using Rankine-Hugoniot relations and assuming that the middle wave (S_M) is a contact discontinuity so that it preserves the associated Riemann invariants. Denoting σ_L, σ_M, $\sigma_R \in \{-1, 0, +1\}$ the signs of the wave speeds S_L, S_M, S_R and $\boldsymbol{F}_L$, $\boldsymbol{F}_L^\star$, $\boldsymbol{F}_R^\star$, $\boldsymbol{F}_R$ the physical fluxes associated to the Riemann states, the HLLC numerical flux writes

$$\boldsymbol{F}_{\text{HLLC}} = \frac{\boldsymbol{F}_L + \boldsymbol{F}_R}{2} - \frac{\sigma_R + \sigma_L}{2} \frac{\boldsymbol{F}_R - \boldsymbol{F}_L}{2} + \frac{\sigma_R - \sigma_L}{2} \frac{\boldsymbol{D}}{2}, \tag{9}$$

where $\boldsymbol{D}$ is the subsonic upwinding ($\boldsymbol{D} = \boldsymbol{0}$ in the supersonic case) which writes

$$\boldsymbol{D} = (\boldsymbol{F}_L^\star - \boldsymbol{F}_L) + (\boldsymbol{F}_R^\star - \boldsymbol{F}_R) - \sigma_M (\boldsymbol{F}_R^\star - \boldsymbol{F}_L^\star) = \begin{bmatrix} D_{\rho Y} & D_{\rho \boldsymbol{u}} & D_{\rho E} \end{bmatrix}^\intercal. \tag{10}$$

Its component $D_{\rho \boldsymbol{u}}$ contains the numerical diffusion on the momentum equation that causes the loss of accuracy in the low-Mach regime. Our low-Mach strategy follows standard approaches available in the literature in that it consists in reducing the numerical diffusion of the pressure terms in the momentum equation, the corrected flux is obtained by adding a supplementary term $\boldsymbol{D}_{\text{sup}}$ to the numerical flux which writes

$$\boldsymbol{D}_{\text{sup}} = (1 - \beta) \left[\rho_L^\star S_L (u_{n,L} - S_M) - \rho_R^\star S_R (S_M - u_{n,R}) \right] \begin{bmatrix} 0 \\ \boldsymbol{n} \\ S_M \end{bmatrix}.$$

In the expression above β is a function that depends on the local Mach number and the role of which is to correctly tune the correction term such that the scheme remains applicable at higher Mach numbers. Several choices of β functions exist and lead to different low-Mach schemes proposed in the literature. In addition to the local Mach numbers, the expression proposed and validated numerically by D. SCHERRER at ONERA also depends on the local pressure jumps, its expression is

$$\beta = \min \left[1, M_L + M_R + \frac{|p_L - p_R|}{\rho_L c_L^2 + \rho_R c_R^2 + \varepsilon} + 10^{-2} \right], \quad \varepsilon = 10^{-10}, \tag{11}$$

with c_L and c_R denoting the sound velocities corresponding to states $\boldsymbol{Q}_L$ and $\boldsymbol{Q}_R$.

We now show the effect of the low-Mach correction on our computations : Figure 1 shows the case of a gas jet impinging a liquid surface, more details on the numerical set-up that we consider are given in the next section. The top row of the figure shows the results with the unmodified HLLC flux while the bottom row corresponds to results with the low-Mach correction. Without any low-Mach treatment strong chequerboard pressure oscillations appear when the acoustic wave from the jet reaches the liquid. When advancing further in time these pressure oscillations see their amplitude grow until reaching negative values

thus crashing the computation. With the low-Mach fix, the pressure fluctuations are controlled and the computation remains stable. We would like to stress that our observations concerning the low-Mach issue differ from those that can be made for Godunov-like schemes applied to the single-phase Euler system. Indeed, for the latter case, it is the strategy which consists in reducing the numerical dissipation in the momentum equation to allow the scheme to recover its accuracy in the low-Mach limit which triggers chequerboard modes when too much numerical viscosity has been removed (Dellacherie 2009). In our case, chequerboard modes appear for the Godunov-like scheme and it is the low-Mach correction which helps removing them, although we observed that small pressure oscillations may still appear sometimes.

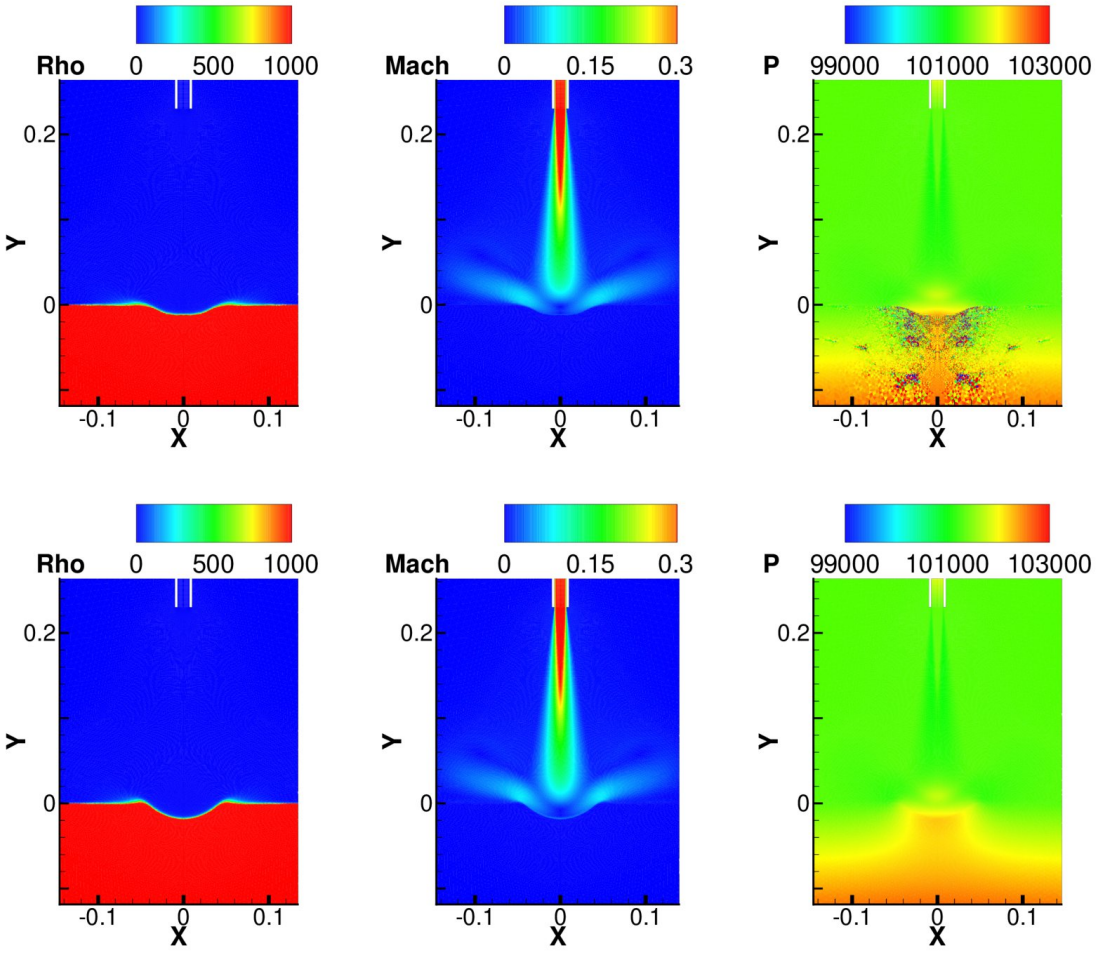

Figure 1: Instantaneous density (left), Mach (middle) and pressure (right) profiles at $t = 3 \cdot 10^{-2}$ s for a mass inflow $\dot{m} = 1.92 \cdot 10^{-2}$ kg/s obtained with the HLLC scheme without any low-Mach correction (top) and with the presented low-Mach fix (bottom) — all other numerical parameters were kept identical. Density scale is in $\mathrm{kg/m^3}$, pressure scale is in Pa while X and Y are scaled in m.

1.4 Numerical set-up

In order to test the capabilities of our model to successfully compute the interface dynamics, we aim at numerically verifying the results presented in Banks and Chandrasekhara (1963) *ie* a relationship between the impinging jet momentum and the depth of the indentation it causes in a liquid interface. We consider the two-dimensional axi-symmetric case, a sketch of the geometry considered is shown in Figure 2 while Table 1 lists the values of the various geometric quantities. The domain is meshed with approximately $55 \cdot 10^3$ cells and using a time-step of $\Delta t = 2.5 \cdot 10^{-6}$ s the simulation is carried over a duration of 4 seconds. The initial condition is that of a horizontal liquid-gas interface located at $y = 0$, the flow field is at rest at hydrostatic pressure. Turbulence in two-phase media is a complex phenomenon which is not the topic of the present study. In order to account for the jet's turbulence the $k - \omega$ model with Sarkar's correction has been used, details and discussions on the turbulence model are given in the Appendix. Eventually, the surface tension fluxes are not taken into account and will remain so throughout the present study. Surface tension will be included in future works since it has an impact on both large scale dynamics as well as small scale atomization and break-up. Rosler and Stewart (1968) exhibited the influence of the critical jet momentum as a

bifurcation parameter dependent on surface tension effects. Above a critical value of this parameter, the cavity becomes unstable and the dynamics of the interface experiences an important change. Also, as the jet momentum increases, the interface's lip will lead to progressive interface atomization and creation of a spray of droplets, a process influenced by surface tension. However, the coupling between interface dynamics, surface tension and turbulence is far from being fully understood in terms of modeling and simulation and thus has not been included in the present study even if it is a work in progress.

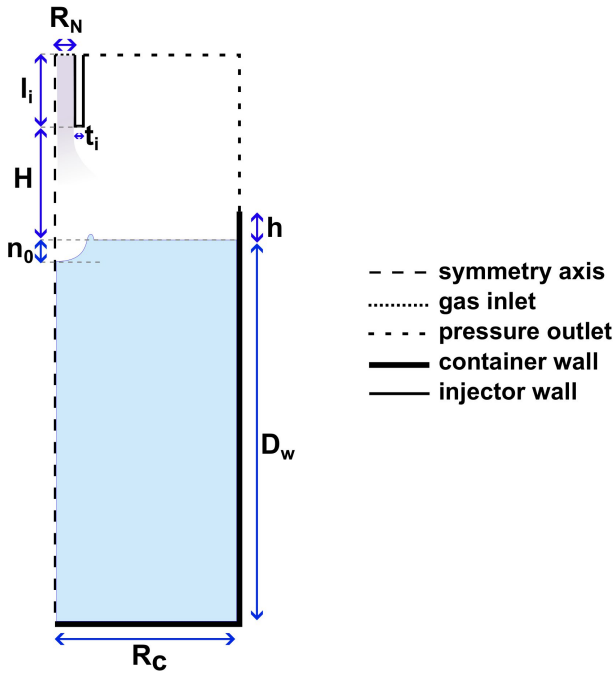

Figure 2: Sketch (not at scale) of a gas jet impinging on a liquid pool : geometrical set-up and notations.

symbol	value (cm)	description	symbol	value (cm)	description
n_0	—	Cavity depth	t_i	0.3	Injector wall thickness
$R_N = {}^{d_N}/_2$	0.7	Nozzle radius	l_i	10	Injector wall length
H	23	Nozzle elevation	h	15	Container wall height
D_w	91	Water depth	$R_c = {}^{d_c}/_2$	38	Container radius

Table 1: Definitions and values of the parameters defining the geometry of the considered set-up.

1.5 Numerical results and discussions

Computations have been done by imposing different mass inflows at the inlet boundary while keeping all other parameters (including mesh and time step) constant. Mass inflow values as well as jet velocities and cavity depths are given in Table 2. Jet Reynolds number ranges from $1.8 \cdot 10^4$ to $1.1 \cdot 10^5$. Four seconds of physical time have been simulated and results have been averaged over the last second, Figure 3 shows the obtained density and Mach number profiles for a mass inflow $\dot{m} = 1.92 \cdot 10^{-2}$ kg/s *ie* for run 6.

Theoretical values of cavity depths are those obtained using the model of Banks and Chandrasekhara (1963). To relate the cavity depth to jet momentum, they propose a stagnation-pressure analysis which relies on the expression of the center-line velocity V_c of a free jet. After a potential core region — whose length is proportional to the nozzle's diameter d_N — the center-line velocity decreases with the distance to the nozzle $H - y$ because of turbulent spreading. For an incompressible axi-symmetric turbulent jet, one has

$$\frac{V_c(y)}{V_{\text{jet}}} = K \frac{d_N}{H - y}, \tag{12}$$

with K being an empirical constant. A table in Banks and Chandrasekhara (1963) summarizes some previous works of the literature where K was obtained experimentally. Typical values lie in between 5 and 8. In our case, fitting (12) (with an offset) for $5 \leq {}^{(H-y)}/_{d_N} \leq 15$ in order to account for the potential core and the displaced liquid regions yields the value of $K = 6.58$. In non-dimensional variables, the profiles corresponding to the highest jet Reynolds' numbers (runs 4 to 6) almost perfectly collapse as shown on Figure 4.

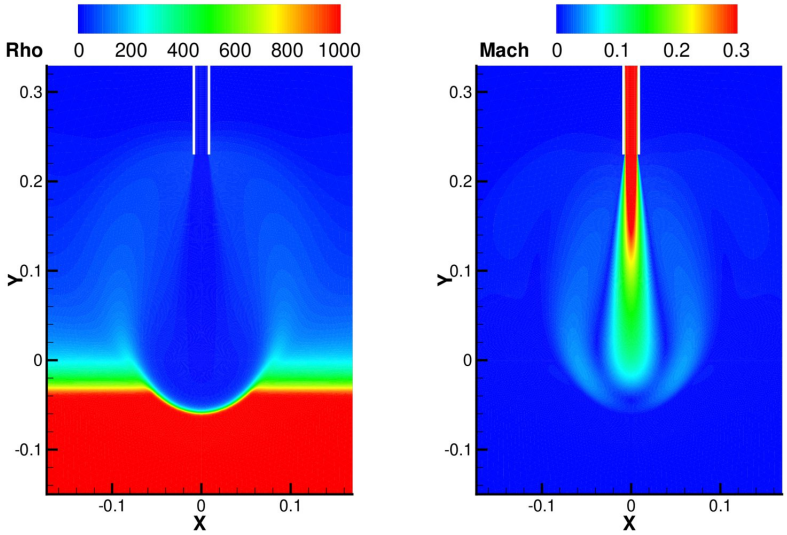

Figure 3: Zoom on the area of interest of the density ($\mathrm{kg/m^3}$) and Mach number profiles for $\dot{m} = 1.92 \cdot 10^{-2}$ kg/s (run 6), profiles are time averaged between $t = 3$ s et and $t = 4$ s.

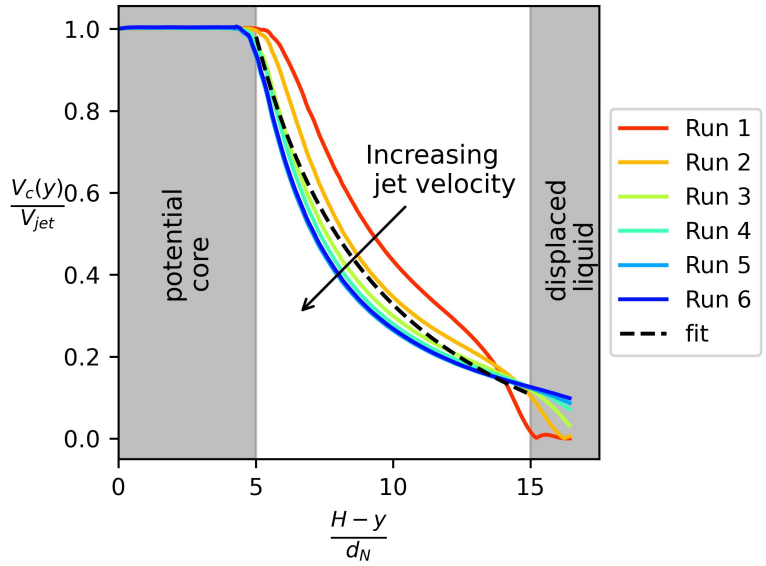

Figure 4: Plot of the center-line jet velocity profiles against the distance to the injector exit z. Colored curves correspond to the different runs while the dashed curve corresponds to the fit $y = {}^{K}/_{x} - c$ for $K = 6.58$ and offset $c = 0.33$.

Cavity depths have been measured using the center-line ($x = 0$) volume fractions : the interface is assumed to be located at height y such that $\alpha(y) = 0.5$ but since for diffuse interface models the interface is spread out, we considered a margin $y \in [y_{\min},\ y_{\max}]$ ensuring $\alpha(y) \in [0.05,\ 0.95]$ (bounds on α were chosen arbitrarily and no other uncertainty analyses such as numerical error estimation or mesh convergence study have been done). The results are plotted against the jet velocity in Figure 5 and listed in Table 2. The error bars on the graph correspond to the margin on the interface location ($y_{\min}$ and $y_{\min}$). We notice that the numerical cavity depths are systematically less deeper than those predicted with a relative error about 25% for the deepest cavities. Using a VOF method and a Piecewise Linear Interface Capture method to reconstruct the interface, Adib et al. (2018) obtained a 14% relative error on cavity depths when comparing their numerical results to their own experimental data, in our case no interface reconstruction techniques are used as we rely on a diffuse interface model. There are several explanations for the observed differences between the numerical results and theoretical predictions : first the mesh we have used might not be sufficiently fine (our mesh has $55 \cdot 10^3$ cells and could be refined more). Second the turbulence model we used is valid in single-phase regions but near the interface it might not be accurate, this could have a major impact as it are the velocity and pressure profiles near the interface that determine the cavity's shape. Finally, the theoretical model does not take

into account viscous effects and thus cavity depths might be slightly over-estimated. Moreover, despite these differences, we do however observe the correct trend for the cavity depth increase with respect to the jet velocity.

	Run 1	**Run 2**	**Run 3**	**Run 4**	**Run 5**	**Run 6**
$\dot{m}_{\text{total}}$ (10^{-3}kg/s)	3.08	6.16	9.24	12.32	15.39	19.24
V_{jet} (m/s)	20.4	39.9	58.9	77.5	95.8	118.2
n_0 (mm)	4.70	9.21	19.12	30.93	42.64	58.36
n_0^{fit} (mm)	3.76	13.26	26.01	40.48	55.51	74.36
relative error (%)	25.28	30.57	26.07	23.59	23.18	21.52

Table 2: Injection conditions and results for the cavity depth obtained for different jet velocities and comparison to the theoretical predictions for $K = 5.52$.

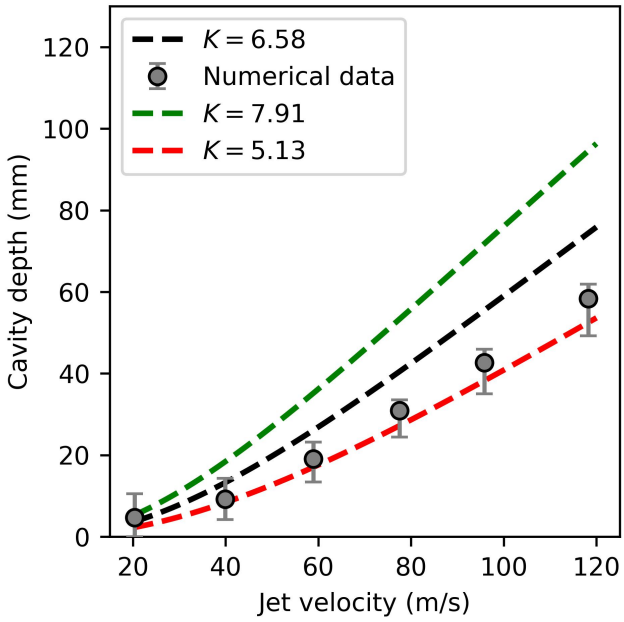

Figure 5: Results for the cavity depth as a function of jet velocity and comparison to theoretical predictions. Values $K = 5.13$ (red) and $K = 7.91$ (green) are the lowest and highest listed values in Banks and Chandrasekhara (1963), while $K = 6.58$ (black) is the value used to fit our numerical velocity profiles.

Before moving on to the following section, which concerns the case of a high-temperature jet, we conclude this section by mentioning that computations in a supersonic jet and oscillating cavity configuration have also been done at ONERA. In this case, the low-Mach issues had a lesser impact on the dynamics than in our case. However, a comparison to experimental data provided by the Direction Générale de l'Armement (French defense procurement and technology agency) showed that the use of the low-Mach correction allowed for better agreement with the data for cavity oscillation amplitude and frequency (Dupays et al. 2021).

2 Extension to the case of a high-temperature jet

2.1 Results with the 4-equation model

We now test our 4-equation model on the case of a hot jet by raising its temperature to $T_{\text{jet}} = 2000$ K while keeping the mass inflow constant (thus raising the inflow velocity and jet Mach number). For this case, the 2^{nd}-order SSP RK method (7) has been used with $m = 21$ stages (as it proved to be more robust than the linearly implict Euler method). The results are shown in Figure 6, we observe that the jet's temperature rapidly decreases once it exits the nozzle. This is due to the important water mass fraction propagation throughout the computational domain, indeed for such a mass fraction imbalance, the thermal equilibrium assumption of the 4-equation model is equivalent to the liquid's temperature being imposed as the mixture temperature. We stress that this is entirely coherent with the thermodynamics of the model as the numerical scheme is conservative with respect to the total energy of the system. It should be noted that this mass fraction propagation already happened in the previous cases but since both phases had the same temperature, it had no effect on the thermodynamics as opposed to the present case.

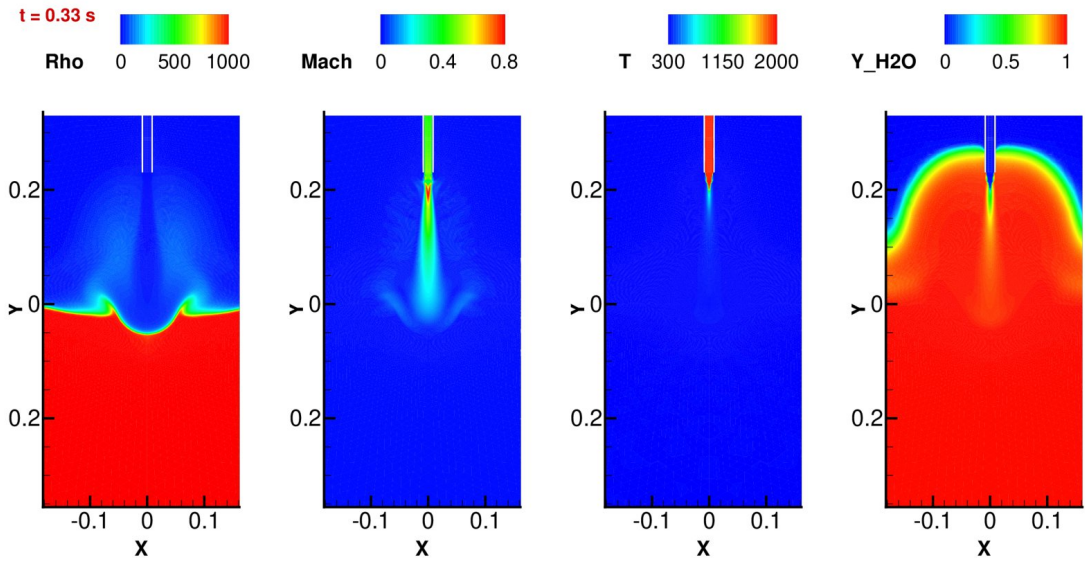

Figure 6: Results for the hot jet case at $t = 0.33$ s.

The reasons for this important mass fraction propagation is because of the strong density ratio between the two phases and the diffuse interface modelling approach. Indeed, since $Y_\ell = 1 - 1/\left(1 + \frac{\alpha_\ell}{\alpha_\mathrm{g}}\frac{\rho_\ell}{\rho_\mathrm{g}}\right)$ with $\rho_\ell/\rho_\mathrm{g} \gtrsim 10^3$, in order to guarantee $Y_\ell \ll \varepsilon$, we must keep $\alpha_\ell/\alpha_\mathrm{g} \sim \alpha_\ell \ll 10^{-3}\varepsilon$. However, as the interface is spread out over what are considered as mixture cells by the model, small amounts of water volume fraction are carried away by the recirculation of the jet. This is amplified in the case of water splashing which occurs at high jet velocities but also by the numerical diffusion on the interface. Figure 7 shows the onset of this effect. Although not used in this paper, techniques such as compressive limitation in the MUSCL reconstruction are being studied and might help counterbalance this effect (Le Touze and Rutard 2022). We conclude this paragraph by pointing out that the specific configuration we use in this contribution, with symmetry and recirculations, is challenging in terms of predicting the proper liquid mass fraction transport and dynamics within the diffuse interface framework. It is especially significative in the turbulent case and RANS approach, where the turbulent mass fluxes near the interface have a strong influence on the global dynamics. A 5-equation model that does not rely on the thermal equilibrium assumption and for which each phase has its own temperature being less sensitive to this issue, the development of such a model is the topic of the rest of this paper.

2.2 Presentation of the 5-equation model and its numerical method

In order to take into account the thermal non-equilibrium that may exist between the two phases, we consider a 5-equation model in which each phase has its own temperature. The model, derived by Kapila et al. (2001), is obtained by considering the 7-equation model of Baer and Nunziato (1986) in the limit of instantaneous velocity and pressure relaxations. Its state vector is $\boldsymbol{Q}^{(5)} = (\alpha_k\rho_k y_{j,k}, \rho\boldsymbol{u}, \rho E, \alpha_\mathrm{g})^\intercal$ and obeys the PDE

$$\partial_t \boldsymbol{Q}^{(5)} + \nabla\cdot\left(\boldsymbol{f}_\mathbf{c}^{(5)} + \boldsymbol{f}_\mathbf{d}^{(5)} + \mathbf{f}_{\boldsymbol{\sigma}}^{(5)}\right) + \boldsymbol{K}^{(5)}\nabla\cdot\boldsymbol{u}^{(5)} = \boldsymbol{S}^{(5)} + \boldsymbol{S}_{\Delta T}^{(5)}. \tag{13}$$

Here $\boldsymbol{K}^{(5)}$ represents the non-conservative convective fluxes, other notations are similar to those used for the 4-equation model, $\boldsymbol{f}_\mathbf{c}^{(5)}$ denotes the conservative convective fluxes

$$\boldsymbol{f}_\mathbf{c}^{(5)} = \boldsymbol{Q}^{(5)}\otimes\boldsymbol{u} + [\mathbf{0},\,\mathbf{0},\,p\mathbf{Id},\,\mathbf{0},\,\mathbf{0}]^\intercal, \qquad \boldsymbol{K}^{(5)} = \left[0,\,0,\,\mathbf{0},\,0,\,\frac{\alpha_\mathrm{g}\rho_\ell c_\ell^2}{\alpha_\ell\rho_\mathrm{g}c_\mathrm{g}^2 + \alpha_\mathrm{g}\rho_\ell c_\ell^2}\right]^\intercal, \tag{14}$$

while $\boldsymbol{f}_\mathbf{d}^{(5)}$ and $\boldsymbol{f}_{\boldsymbol{\sigma}}^{(5)}$ correspond to the diffusive and surface tension fluxes (we recall that in the present study, surface tension effects are neglected). Source terms such as body forces are represented by $\boldsymbol{S}^{(5)}$ while the new term $\boldsymbol{S}_{\Delta T}^{(5)}$ represents the interface fluxes associated to the thermal non-equilibrium between the two phases such as heat transfer and evaporation. Provided that the equation of state of each phase is given, the equilibrium pressure is determined by solving

$$Y_\mathrm{g}e_\mathrm{g}^\mathrm{EOS}(p,\rho_\mathrm{g}) + Y_\ell e_\ell^\mathrm{EOS}(p,\rho_\ell) = e. \tag{15}$$

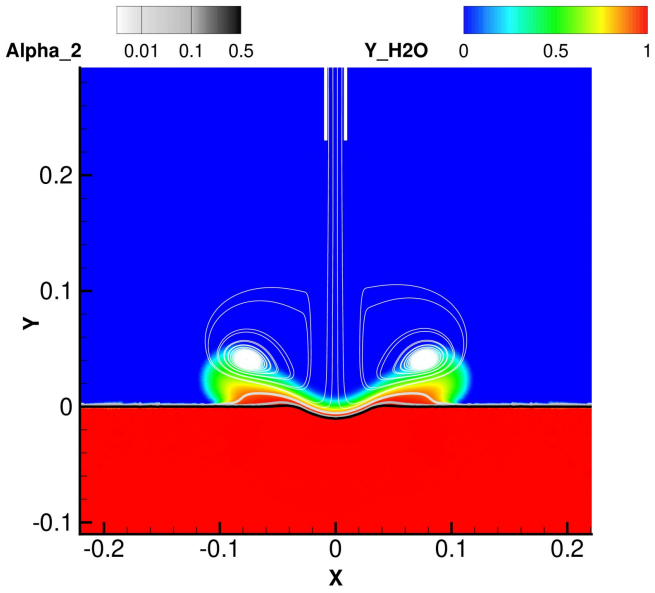

Figure 7: Zoom on the area of interest of the instantaneous water mass fraction Y_ℓ profile at time $t = 6 \cdot 10^{-3}$ s. Thin white lines represent velocity streamlines while grey-scale contour levels represent water volume fractions at $\alpha_\ell = 0.5$ (black), $\alpha_\ell = 0.1$ (grey) and $\alpha_\ell = 0.01$ (silver).

This model however is quite challenging from a numerical point of view. The non-conservative term in the volume fraction equation does not allow to define jump conditions for shocks and the positivity of the volume fraction is not always guaranteed by the usual schemes. An interesting numerical strategy is the use of relaxation schemes by considering an out-of-pressure-equilibrium-6-equation model for which the solutions converge to the ones of the 5-equation model in the case of an instantaneous pressure relaxation. First introduced by Saurel et al. (2009), this strategy has been revisited by several authors (Pelanti and Shyue 2014; Schmidmayer et al. 2017). The 6-equation model we consider here is the one derived in the PhD of P. Cordesse (2020), the full model contains sub-scale geometric quantities. When neglecting sub-scale quantities, the variables reduce to $\boldsymbol{Q}^{(6)} = (\alpha_k \rho_k y_{j,k}, \rho \boldsymbol{u}, \alpha_k \rho_k e_k, \alpha_g)^\intercal$ and are solutions of

$$\partial_t \boldsymbol{Q}^{(6)} + \nabla \cdot \left(\boldsymbol{f}_{\mathbf{c}}^{(6)} + \boldsymbol{f}_{\mathbf{d}}^{(6)} + \mathbf{f}_{\boldsymbol{\sigma}}^{(6)} \right) + \boldsymbol{K}_{\mathbf{c}}^{(6)} \nabla \cdot \boldsymbol{u}^{(6)} + \underline{\underline{\mathbf{K}}}_d^{(6)} : \nabla \boldsymbol{u}^{(6)} = \boldsymbol{S}^{(6)} + \boldsymbol{S}_{\Delta T}^{(6)} + \frac{\boldsymbol{R}\left(\boldsymbol{Q}^{(6)}\right)}{\varepsilon}. \tag{16}$$

The conservative and non-conservative convective fluxes are given by

$$\boldsymbol{f}_{\mathbf{c}}^{(6)} = \boldsymbol{Q}^{(6)} \otimes \boldsymbol{u} + [\mathbf{0},\, \mathbf{0},\, p\mathbf{Id},\, \mathbf{0},\, \mathbf{0}]^\intercal, \qquad \boldsymbol{K}_{\mathbf{c}}^{(6)} = [0,\, 0,\, \mathbf{0},\, \alpha_g p_g,\, \alpha_\ell p_\ell,\, \alpha_g]^\intercal. \tag{17}$$

The mixture pressure in the momentum flux is given by $p = \alpha_g p_g + \alpha_\ell p_\ell$. Once again $\boldsymbol{f}_{\mathbf{d}}^{(6)}$, $\boldsymbol{f}_{\boldsymbol{\sigma}}^{(6)}$ and $\boldsymbol{S}^{(6)}$ denote the diffusive, capillary fluxes and body forces while $\boldsymbol{S}_{\Delta T}^{(6)}$ represent thermal disequilibrium terms. Because the energy equations are on the internal energies, non-conservative diffusive term appear and are represented by the third-order tensor $\underline{\underline{\mathbf{K}}}_d^{(6)}$, details on the diffusive fluxes can be found in Schmidmayer et al. (2016). The relaxation term which pushes the system towards pressure equilibrium writes

$$\boldsymbol{R}\left(\boldsymbol{Q}^{(6)}\right) = [0,\, 0,\, \mathbf{0},\, p(p_\ell - p_g),\, p(p_g - p_\ell),\, (p_g - p_\ell)]^\intercal. \tag{18}$$

Because for this model each phase has its own pressure and temperature, their thermodynamics closures are independent and given by

$$p_k = p_k^{\mathrm{EOS}}(\rho_k, e_k), \qquad T_k = T_k^{\mathrm{EOS}}(\rho_k, e_k), \qquad e_k = e_k^{\mathrm{EOS}}(p_k, T_k). \tag{19}$$

Since one has $\lim_{\varepsilon \to 0} \boldsymbol{Q}_\varepsilon^{(6)} = \boldsymbol{Q}^{(5)}$, the 6-equation model is used to design a numerical scheme for the 5-equation model. The scheme is based on two building blocks : Starting from $\boldsymbol{Q}^{(5),n}$ we do a convection step where the unknowns are updated according to the 6-equation model without any relaxation terms using the HLLC flux, then $\boldsymbol{Q}^{(5),n+1}$ is obtained through a projection step by means of an instantaneous relaxation to restore the pressure equilibrium and determine the corresponding volume fraction.

Because in the 6-equation model we solve the internal energy equation for each phase, the numerical discretization might not be fully conservative with respect to the total energy of the mixture. To overcome this problem, one can use a formulation of the 6-equation model based on the total energies of each phase which allows the design of numerical schemes which are conservative for the total energy of the mixture, see for instance Pelanti and Shyue (2014). Another approach, and the one we

follow, is the one presented in Saurel et al. (2009), and which consists in adding the total energy equation to the system (17). This equation is of course redundant for smooth solutions in the continuous case but is used after the relaxation step to ensure the strict conservation of the total energy. Using superscript (1) to denote quantities obtained after the relaxation step and (0) to denote quantities unaffected by the relaxation, the procedure consists in finding $p^{(2)}$ such that

$$\sum_{k=\mathrm{g},\ell} \left(\alpha_k \rho_k\right)^{(0)} e_k^{\mathrm{EOS}}\left(p^{(2)}, \rho_k^{(1)}\right) = \left(\rho E - \frac{1}{2}\rho \boldsymbol{u}^2\right)^{(0)}. \tag{20}$$

We draw the reader's attention to the fact that although both systems are hyperbolic with simple eigenvalues $\lambda = \boldsymbol{u}\cdot\boldsymbol{n} \pm c$ and non-simple eigenvalues $\lambda = \boldsymbol{u}\cdot\boldsymbol{n}$, they do not share the same mixture sound velocity since

$$\left(\rho c^2\right)^{(5)} = \rho c^2_{\mathrm{equilibrium}} = \left(\frac{\alpha_g}{\rho_g c_g^2} + \frac{\alpha_\ell}{\rho_\ell c_\ell^2}\right)^{-1}, \qquad \left(\rho c^2\right)^{(6)} = \rho c^2_{\mathrm{frozen}} = \alpha_g \rho_g c_g^2 + \alpha_\ell \rho_\ell c_\ell^2. \tag{21}$$

Moreover, although the numerical strategy yields a scheme for the 5-equation model, the convection step uses the 6-equation model and therefore CFL conditions are based on c_{frozen} instead of $c_{\mathrm{equilibrium}}$ (also referred to as Wood's velocity c_{wood}). Notice that for the same mixture conditions (identical α, ρ_{g} and ρ_ℓ), we always have $c_{\mathrm{frozen}} \geq c_{\mathrm{equilibrium}}$. This stems from the so-called sub-characteristic condition — eigenvalues of the system to be solved must lie in between those of the relaxation system — which is a requirement for the stability of the method (Liu 1987; Jin and Xin 1995).

Considering relaxation systems for which instantaneous relaxation is achieved by means of a linear projection and for which the equilibrium is parametrized by a Maxwellian, Bouchut (2004) showed that projecting the solution of an approximate Riemann solver applied to two equilibrium states yields an approximate Riemann solver for the equilibrium (or relaxed) system. As a consequence, when using a Godunov-like scheme in the convection step, the "convection + projection" scheme is equivalent to a Godunov-like scheme for the relaxed system using this newly defined approximate Riemann solver.

Based on these considerations we assume that our numerical strategy for the 5-equation system can be interpreted as a single explicit Euler step for a Godunov-like scheme with an implicitly defined Riemann solver. Higher order time integration can then be achieved by means of a Runge-Kutta method. The resulting scheme is not a splitting scheme as instantaneous relaxations are performed at each intermediate stage. This is a requirement to guarantee higher order accuracy since classical splitting schemes (even higher order splittings) are subject to a loss of accuracy in the limit of an instantaneous relaxation (Jin 1995).

The development of this 5-equation model is still a work in progress, future works will include the modelling of sub-scale geometric quantities such as the interfacial area density Σ or mean interface curvature. Access to such quantities will allow for an accurate modelling of thermal source terms $\boldsymbol{S}_{\Delta t}$ such as the heat flux between phases, which will be of the form $h\Sigma(T_{\mathrm{g}} - T_\ell)$ with h the heat transfer coefficient, but also phase change modelling and surface tension effects.

We conclude this section by mentioning that since the convective part of the 6-equation model is discretized similarly to the previous 4-equation model, the low-Mach correction has been easily adapted. We now move on to the next section where we propose a numerical comparison between the considered models.

2.3 Comparison to the previous model on a simplified set-up

As the development of the proposed 5-equation model is a work still in progress, we now propose a numerical comparison between the two models on a simplified set-up. Since the main objective of this part is to compare the thermodynamic behaviour of the models, the simplified test case remains of interest even if it is no longer physically representative. The changes compared to the previous set-up are :

- Single species for each phase, we consider a water-nitrogen system.
- No heat diffusion terms in the 5-equation model yet, to account for this they have also be set to zero in the 4-equation model.
- No sub-scale quantities : although transport equations on sub-scale quantities have been derived (Cordesse 2020; Di Battista 2021), no source terms have been added yet as such they do not contribute to the flow.
- No heat exchange between phases source terms $\boldsymbol{S}_{\Delta T}$ still need to be modelled and therefore for the 5-equation model we have an infinitely slow temperature relaxation whereas the 4-equation model considers infinitely fast temperature relaxations.
- No turbulence terms are included. This has a strong impact on the dynamics. In the absence of turbulent spreading, the cavity will lose its parabolic shape and it changes velocity profile : whereas previously the recirculation induces a shear flow along the interface, the recirculation will now redirect the flow in the vertical direction. This will change the way liquid mass fraction is ripped of the interface and propagates through the domain.

Again we use the 2^{nd}-order SSP RK with $m = 21$ stages, the gas is injected at 1000 K and with a velocity of 20 m/s. The results for the 4-equation model on this new set-up are shown in Figure 8, once again the model suffers from an important mass fraction propagation which in turn leads to unphysical temperatures. For the 5-equation model, results are shown in Figure 9, the temperature field that is shown corresponds to a mixture temperature T_{mixture} that is defined as follows

$$T_{\text{mixture}} = \frac{Y_{\text{g}} c_{p,\text{g}} T_{\text{g}} + Y_{\ell} c_{p,\ell} T_{\ell}}{Y_{\text{g}} c_{p,\text{g}} + Y_{\ell} c_{p,\ell}}. \tag{22}$$

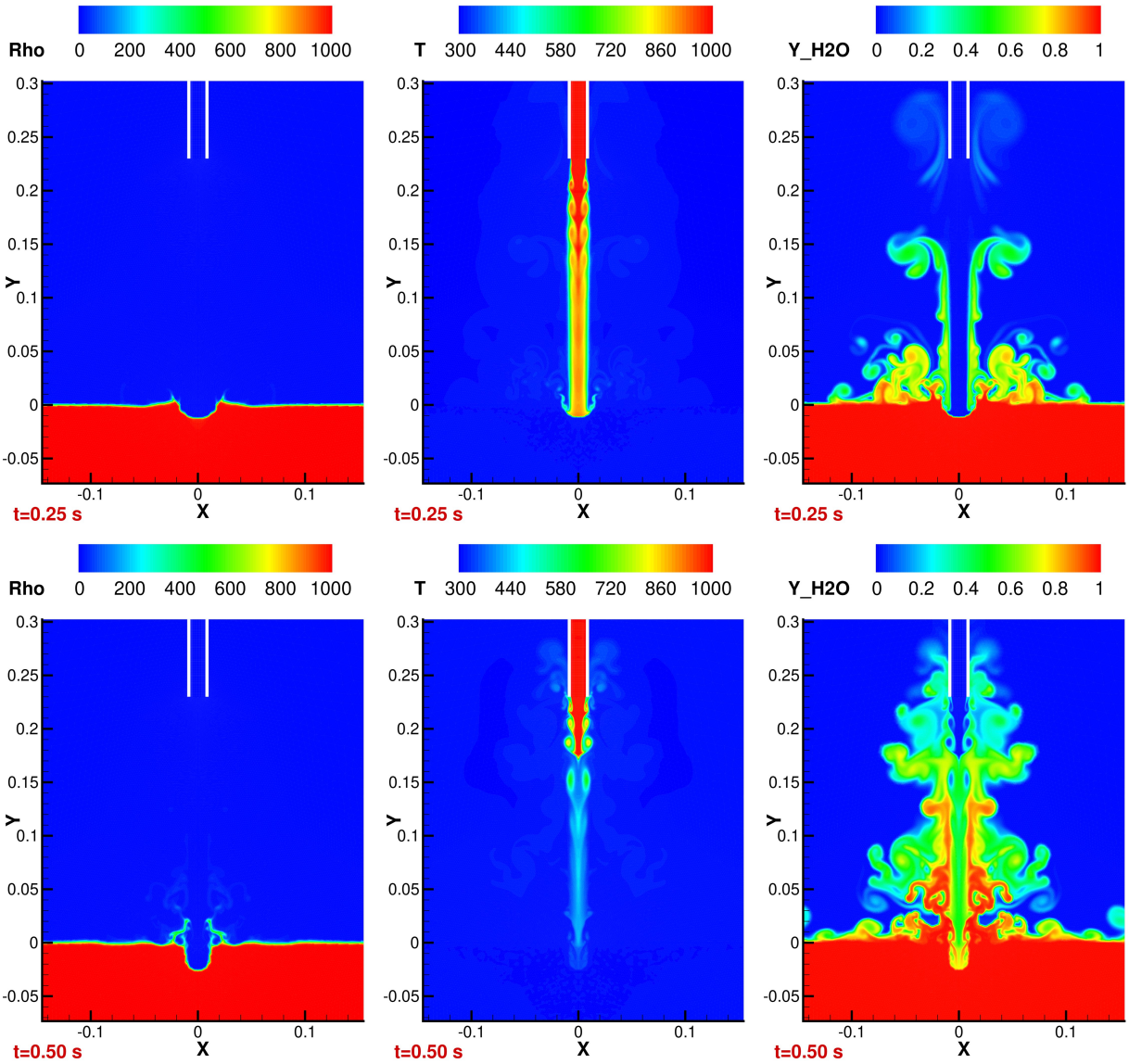

Figure 8: Density, temperature and liquid mass fractions at $t = 0.25$ s (top row) and $t = 0.5$ s (bottom row) obtained with the 4-equation model.

We would like to stress that since no heat exchange terms are present, the jet naturally preserves its temperature, but since the internal energies of each phase are now properly resolved, the mixture temperature is also preserved (despite the mass fraction propagation). Figures 8 and 9 also show that the two models predict different cavities. This difference also originates from the temperature equilibrium assumption : the instantaneous cooling of the jet in the 4-equation model leads to a higher density of the jet and thus an excessively deep cavity. Not based on this thermal equilibrium assumption, the 5-equation model provides the proper framework to model heat exchange between phases. If the heat exchange terms are not properly modelled, the mass fraction propagation may lead to distorted temperature fields as for the 4-equation model. To avoid this our strategy consists in the development of an equation on the interfacial area density Σ which will allow us to modulate the intensity of heat exchanges.

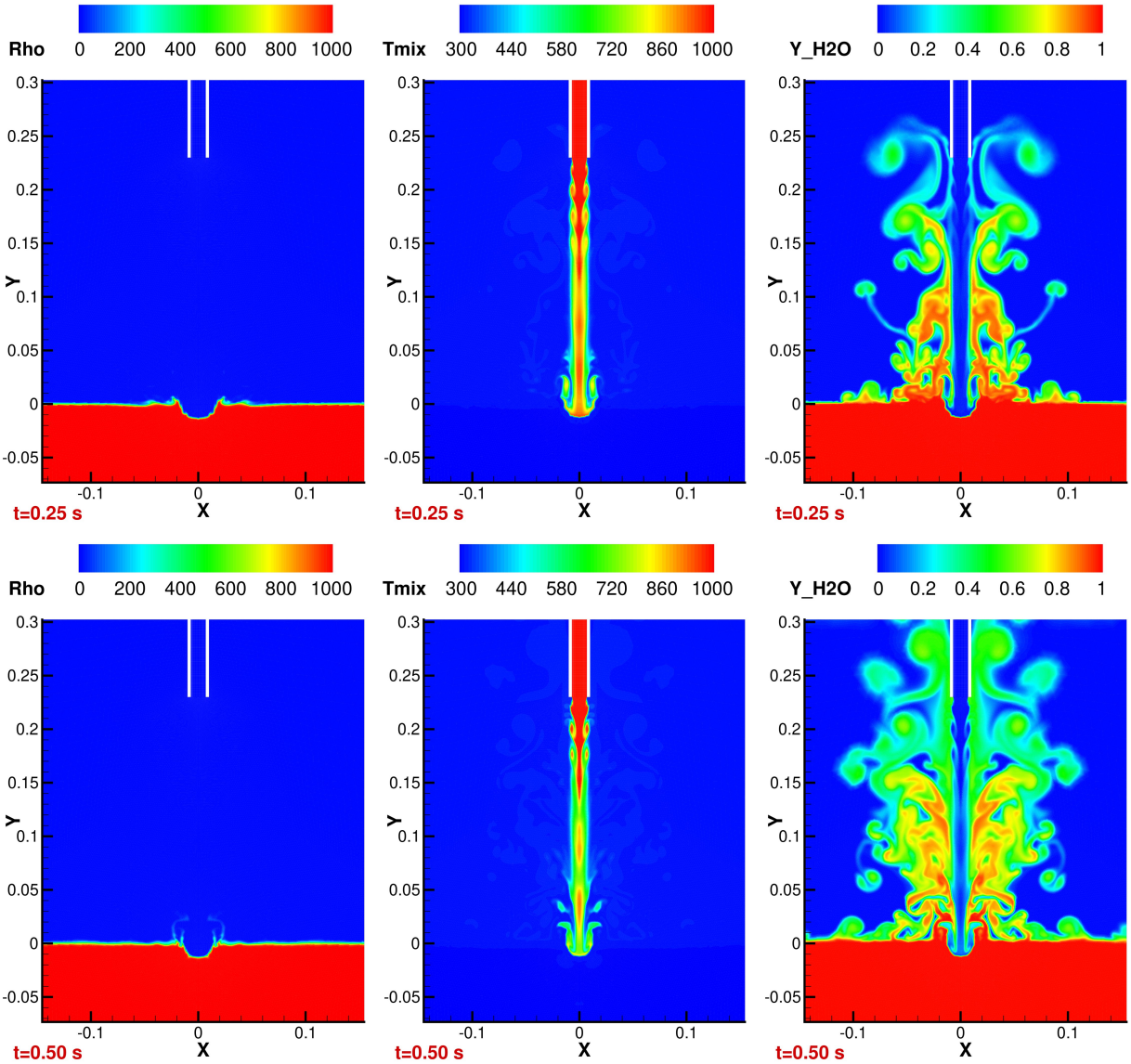

Figure 9: Density, temperature and liquid mass fractions at $t = 0.25$ s (top row) and $t = 0.5$ s (bottom row) obtained with the 5-equation model.

Conclusion

In this work we investigated the numerical simulation of a gaseous jet impacting a liquid surface using diffuse interface models. Because of the low compressibility of the liquid which is initially at rest, non-physical pressure oscillations appear and render the computation unstable. The use of a scheme adapted to the low-Mach regime allows to recover the stability even though we observed that small pressure oscillations may still appear (but remain bounded). Using a 4-equation model which assumes local pressure, velocity and temperature equilibrium between both phases, simulations have been carried out for different jet velocities. The depths of the cavities formed by the impinging jet have been compared to theoretical data.

Because of the complex flow pattern, the diffuse interface approach and the strong density jump between the phases, liquid mass fraction propagates throughout the computational domain even where the volume fraction is negligible. Combined with thermal equilibrium assumption of the 4-equation model, this leads to non-physical temperature profiles in the case of a hot jet. The development of a 5-equation model for which the thermal equilibrium assumption is lifted allows to overcome the thermodynamical problems related to this mass fraction propagation. Further works will include the development of the full 5-equation model for which sub-scale geometric quantities will be included to enrich the model, allow for a better description of turbulent fluctuations near the interface and take into account the dispersed phase composed water droplets.

Acknowledgements

The authors would like to thank the Agence de l'Innovation de Défense (AID) for its support through a PhD grant for W. Haegeman and acknowledge Jean-Baptiste Deuff for his role as technical advisor.

Appendix

In order to take into account turbulent fluctuations in the momentum equation, we use the Boussinesq assumption by considering that the Reynolds' stress tensor $R_{ij} := -\bar{\rho}\widetilde{u_i''u_j''}$, writes

$$R_{ij} = 2\mu_t D_{ij} - \frac{2}{3}\rho k\delta_{ij}, \qquad \text{with } \boldsymbol{D} = \frac{1}{2}\left(\nabla\boldsymbol{u} + \nabla\boldsymbol{u}^{\intercal}\right) - \frac{1}{3}(\nabla\cdot\boldsymbol{u})\mathbf{Id}. \tag{23}$$

Here $\boldsymbol{D}$ is the traceless part of the strain tensor while k and μ_t are the turbulent kinetic energy (TKE) and turbulent viscosity respectively. We have also used the standard notations $\bar{\bullet}$ to denote the ensemble average, $\tilde{\bullet}$ to denote the Favre average, *ie* density weighted average, and $\bullet''$ to designate a variable's fluctuations with respect to its Favre average.

Following the SST $k-\omega$ model with Sarkar's compressibility correction, we assume that the turbulent viscosity is a function of k and the specific dissipation rate ω, such that

$$\mu_t = \frac{a_1\rho k}{\max(a_1\omega, \Omega F_2)}. \tag{24}$$

Here $\Omega = |\nabla\times\boldsymbol{u}| = \sqrt{2\boldsymbol{\Omega}:\boldsymbol{\Omega}}$ is the vorticity's magnitude ($\boldsymbol{\Omega}$ being the antisymmetric part of the velocity gradient), while $a_1 = 0.31$ and F_2 is a blending function depending also on the distance to the wall y_{w} and the dynamic viscosity μ. It writes

$$F_2 = \tanh\left(\Gamma_2^2\right) \qquad \text{with } \Gamma_2 = \max\left[\frac{2\sqrt{k}}{0.09\omega y_{\mathrm{w}}}, \frac{500\mu}{\rho\omega y_{\mathrm{w}}^2}\right]. \tag{25}$$

The system is closed by the following equations

$$\left\{\begin{array}{rcl} \rho\dfrac{\mathrm{D}k}{\mathrm{D}t} &=& \nabla\cdot[(\mu+\sigma_k\mu_t)\nabla k] \;+\; (1-\alpha_1 M_t^2)P_k \;-\; (1+\alpha_2 M_t^2)\beta^\star\rho k\omega \;-\; \dfrac{1}{\mathrm{Pr}_t}\dfrac{g\mu_t}{\rho}\left.\dfrac{\partial\rho}{\partial T}\right|_p\dfrac{\partial T}{\partial y} \\ \rho\dfrac{\mathrm{D}\omega}{\mathrm{D}t} &=& \nabla\cdot[(\mu+\sigma_\omega\mu_t)\nabla\omega] \;+\; \dfrac{\rho\gamma}{\mu_t}P_k \;-\; \beta\rho\omega^2 \;+\; 2\rho(1-F_1)\dfrac{\sigma_{\omega,2}}{\omega}\nabla k\cdot\nabla\omega \end{array}\right. \tag{26}$$

for which the production term P_k writes

$$P_k = \max\left[\min\left(\Pi_k,\ 20\beta^\star\rho k\omega\right),\ 0\right], \qquad \text{with } \Pi_k = \mu_t\boldsymbol{D}:\boldsymbol{D} - \frac{2}{3}\rho k(\nabla\cdot\boldsymbol{u}). \tag{27}$$

In these equations, F_1 is another blending function such that for $\mathcal{X}\in\{\sigma_k,\,\sigma_\omega,\,\beta,\,\gamma\}$, we have $\mathcal{X} = F_1\mathcal{X}_1 + (1-F_1)\mathcal{X}_2$ with

$$\begin{array}{rlllll} \mathcal{X}_1 \;:& \sigma_{k1} = 0.85, & \sigma_{\omega 1} = 0.5, & \beta_1 = 0.0750, & \gamma_1 = \dfrac{\beta_1}{\beta^\star} - \dfrac{\sigma_{\omega 1}\kappa^2}{\sqrt{\beta^\star}}, \\ \mathcal{X}_2 \;:& \sigma_{k2} = 1.0, & \sigma_{\omega 2} = 0.856, & \beta_2 = 0.0828, & \gamma_2 = \dfrac{\beta_2}{\beta^\star} - \dfrac{\sigma_{\omega 2}\kappa^2}{\sqrt{\beta^\star}}. \end{array} \tag{28}$$

The von Kármán constant is $\kappa = 0.41$ while $\beta^\star = 0.09$. The turbulent Prandtl number is $\mathrm{Pr}_t = 0.9$ and appears in the last term of the TKE equation which models the effects of natural convection. The blending function F_1 is defined as follows

$$F_1 = \tanh\left(\Gamma_1^4\right), \quad \Gamma_1 = \min\left[\max\left(\frac{\sqrt{k}}{0.09\omega y_{\mathrm{w}}}, \frac{500\mu}{\rho\omega y_{\mathrm{w}}^2}\right), \frac{4\rho\sigma_{\omega,2}}{CD_{k\omega}y_{\mathrm{w}}^2}\right], \quad CD_{k\omega} = \max\left(2\rho\frac{\sigma_{\omega,2}}{\omega}\nabla k\cdot\nabla\omega, 10^{-20}\right). \tag{29}$$

Sarkar's compressibility correction consists in modulating the amplitude of the production and dissipation terms in the TKE equation based on a turbulent Mach number, the corresponding coefficients are

$$M_t = \frac{\sqrt{2k}}{c}, \qquad \alpha_1 = 0.15, \quad \alpha_2 = 0.30, \tag{30}$$

with c denoting the local sound velocity.

Turbulent fluctuations in the energy equation are taken into account by modelling the energy flux fluctuations $-\bar{\rho}\widetilde{u_i''h''}$ using a Fourier law such that

$$-\bar{\rho}\widetilde{u_i''h''} = \frac{c_p\mu_t}{\mathrm{Pr}_t}\frac{\partial T}{\partial x_i}. \tag{31}$$

Here c_p is the mixture's heat capacity while Pr_t is the turbulent Prandtl number which has already been introduced. Concerning the mass equations, turbulent mixing due to the fluctuations $-\bar{\rho}\widetilde{u_i''Y_{j,k}}$ is modelled using a Fick law based on a turbulent Schmidt number $\mathrm{Sc}_t = 0.9$ such that

$$-\bar{\rho}\widetilde{u_i''Y_{j,k}} = \frac{\mu_t}{\mathrm{Sc}_t}\frac{\partial Y_{j,k}}{\partial x_i}. \tag{32}$$

This model of turbulent mixing has been derived in a multi-species Navier-Stokes context, it takes into account the turbulent mixing of different species within each phase. In a two-phase flow context, this term also causes a mixing of the two phases at the interface, its validity to model this mixing between phases however is unclear. A complete description of turbulent mixing would require a model to account for turbulent mixing of the phases at the interface based on a critical Weber number as is proposed in Vallet et al. (2001) but is not included here. We also point out that for molecular mixing, our model relies on the gradients of $y_{j,k}$, the mass fraction of a species with respect to its own phase so that molecular diffusion does not lead to a mixing of the different phases.

Turbulence models rely on the fine tuning of a great number of parameters which is done by comparison to DNS data or experimental correlations obtained generally in the case of single-phase flows. Therefore, the turbulence models we use only have a limited validity near the interface. In Adib et al. (2018), an extra term is added to the equation on ω to account for turbulence damping near the interface and to counter for spurious eddy viscosity generated by strong velocity gradients at the interface. In our case, no such corrections terms were added and the turbulence model was used as presented.

References

Adib, M., Ehteram, M. A., Basirat Tabrizi, H., Numerical and Experimental Study of Oscillatory Behavior of Liquid Surface Agitated by High-Speed Gas Jet, *Applied Mathematical Modelling*, vol 62, pp. 510–525, 2018.

Baer, M. R., Nunziato, J. W., A Two-Phase Mixture Theory for the Deflagration-to-Detonation Transition (DDT) in Reactive Granular Materials, *International Journal of Multiphase Flow*, vol 12, no. 6, pp. 861–889, 1986.

Banks, R. B., Chandrasekhara, D. V., Experimental Investigation of the Penetration of a High-Velocity Gas Jet through a Liquid Surface, *Journal of Fluid Mechanics*, vol 15, no. 1, pp. 13–34, 1963.

Bouchut, F., *Nonlinear Stability of Finite Volume Methods for Hyperbolic Conservation Laws*, Basel: Birkhäuser, 2004.

Cheslak, F. R., Nicholls, J. A., Sichel, M., Cavities Formed on Liquid Surfaces by Impinging Gaseous Jets, *Journal of Fluid Mechanics*, vol 36, no. 1, pp. 55–63, 1969.

Cordesse, P., Contribution to the Study of Combustion Instabilities in Cryotechnic Rocket Engines : Coupling Diffuse Interface Models with Kinetic-Based Moment Methods for Primary Atomization Simulations, PhD, Université Paris-Saclay, 2020.

Dellacherie, S., Checkerboard Modes and Wave Equation, *Proc. of Algoritmy, 18th Conference on Scientific Computing*, Podbanské, Slovakia, 2009, pp. 71–80.

Dellacherie, S., Analysis of Godunov Type Schemes Applied to the Compressible Euler System at Low Mach Number, *Journal of Computational Physics*, vol 229, no. 4, pp. 978–1016, 2010.

Di Battista, R., Towards a Unified Eulerian Modeling Framework for Two-Phase Flows : Geometrical Small Scale Phenomena and Associated Flexible Computing Strategies, PhD, Institut Polytechnique de Paris, 2021.

Dupays, J., et al., Rapport de Synthèse AFPPS2, Tranche TC5, RS.10.24M-o, Travaux Sur La Thématique Bulle de Culot, ONERA, France, Technical Report RT 1/26455 DMPE, Oct. 2021.

Gottlieb, S., Ketcheson, D., Shu, C.-W., *Strong Stability Preserving Runge-Kutta and Multistep Time Discretizations*, World Scientific, 2011.

Guillard, H., Viozat, C., On the Behaviour of Upwind Schemes in the Low Mach Number Limit, *Computers & Fluids*, vol 28, no. 1, pp. 63–86, 1999.

Hairer, E., Wanner, G., *Solving Ordinary Differential Equations II*, Heidelberg: Springer Berlin, second edition, 1996.

Jin, S., Runge-Kutta Methods for Hyperbolic Conservation Laws with Stiff Relaxation Terms, *Journal of Computational Physics*, vol 122, pp. 51–67, 1995.

Jin, S., Xin, Z., The Relaxation Schemes for Systems of Conservation Laws in Arbitrary Space Dimensions, *Communications on Pure and Applied Mathematics*, vol 48, 1995.

Kapila, A. K., Menikoff, R., Bdzil, J. B., Son, S. F., Stewart, D. S., Two-Phase Modeling of Deflagration-to-Detonation Transition in Granular Materials: Reduced Equations, *Physics of Fluids*, vol 13, no. 10, pp. 3002–3024, 2001.

Ketcheson, D. I., Highly Efficient Strong Stability Preserving Runge-Kutta Methods with Low-Storage Implementations, *SIAM Journal on Scientific Computing*, vol 30, no. 4, pp. 2113–2136, 2008.

Le Touze, C., Couplage entre Modèles Diphasiques à « Phases Séparées » et à « Phase Dispersée » pour la Simulation de l'Atomisation Primaire en Combustion Cryotechnique, PhD, Université Nice Sophia Antipolis, 2015.

Le Touze, C., Rutard, N., Numerical Methods for Diffuse Interface Multifluid Models, *Proc. of 8th European Congress on Computational Methods in Applied Sciences and Engineering*, Oslo, Norway, 2022.

Liu, T.-P., Hyperbolic Conservation Laws with Relaxation, *Communications in Mathematical Physics*, vol 108, no. 1, pp. 153–175, 1987.

Loison, A., Kokh, S., Pichard, T., Massot, M., A two-scale two-phase flow model with capillarity and small-scale reduced-order model based on a geometric method of moments, presented at, *11th International Conference on Multiphase Flow*, Kobe, Japan, 2023a.

Loison, A., Pichard, T., Kokh, S., Massot, M., Two-scale modelling of two-phase flows with Hamilton's Stationary Action Principle and Geometric Method of Moments, *Journal of Fluid Mechanics*, 2023b, submitted, available on HAL.

Mirjalili, S., Jain, S., Dodd, M., Interface-Capturing Methods for Two-Phase Flows: An Overview and Recent Developments, *Center for Turbulence Research - Annual research brief*, pp. 117–135, 2017.

Molloy, N. A., Impinging Jet Flow in a Two-Phase System : The Basic Flow Pattern, *Journal of the iron and steel institute*, vol 208, pp. 943–950, 1970.

Nguyen, A. V., Evans, G. M., Computational Fluid Dynamics Modelling of Gas Jets Impinging onto Liquid Pools, *Applied Mathematical Modelling*, vol 30, no. 11, pp. 1472–1484, 2006.

Pelanti, M., Shyue, K.-M., A Mixture-Energy-Consistent Six-Equation Two-Phase Numerical Model for Fluids with Interfaces, Cavitation and Evaporation Waves, *Journal of Computational Physics*, vol 259, pp. 331–357, 2014.

Rieper, F., A Low-Mach Number Fix for Roe's Approximate Riemann Solver, *Journal of Computational Physics*, vol 230, no. 13, pp. 5263–5287, 2011.

Rosler, R. S., Stewart, G. H., Impingement of Gas Jets on Liquid Surfaces, *Journal of Fluid Mechanics*, vol 31, no. 1, pp. 163–174, 1968.

Ruuth, S., Spiteri, R., Ruuth, J., A New Class of Optimal High-Order Strong-Stability-Preserving Time Discretization Methods, *SIAM J. Numer. Anal.*, vol 40, 2002.

Saurel, R., Petitpas, F., Berry, R. A., Simple and Efficient Relaxation Methods for Interfaces Separating Compressible Fluids, Cavitating Flows and Shocks in Multiphase Mixtures, *Journal of Computational Physics*, vol 228, no. 5, pp. 1678–1712, 2009.

Schmidmayer, K., Petitpas, F., Daniel, E., A Model and Numerical Method for High Speed Flows with Capillary, Viscous and Heat Conduction Effects, *Proc. of the 46th AIAA Fluid Dynamics Conference*, Washington, D.C., US: American Institute of Aeronautics and Astronautics, 2016.

Schmidmayer, K., Petitpas, F., Daniel, E., Favrie, N., Gavrilyuk, S., A Model and Numerical Method for Compressible Flows with Capillary Effects, *Journal of Computational Physics*, vol 334, pp. 468–496, 2017.

Toro, E. F., Spruce, M., Spears, W., Restoration of the Contact Surface in the HLL Riemann Solver, *Shock Waves*, vol 4, pp. 25–34, 1994.

Vallet, A., Burluka, A. A., Borghi, R., Development of a Eulerian Model for the Atomization of a Liquid Jet, *Atomization and Sprays*, vol 11, no. 6, 2001.